Type II Bi$_{1-x}$W$_x$O$_{1.5+1.5x}$: a (3 + 3)-dimensional commensurate modulation that stabilizes the fast-ion conducting delta phase of bismuth oxide

Julia Wind,[a] Josie E. Auckett,[a] Ray L. Withers,[b] Ross O. Piltz,[c] Andrey Maljuk[d] and Chris D. Ling[a]*

[a]School of Chemistry, The University of Sydney, Sydney, NSW 2006, Australia, [b]Research School of Chemistry, Australian National University, Canberra, ACT 0200, Australia, [c]The Bragg Institute, Australian Nuclear Science and Technology Organization, New Illawara Road, Lucas Heights, NSW 2234, Australia, and [d]Leibniz Institute for Solid State and Materials Research Dresden, Helmholtzstrasse 20, Dresden D-01069, Germany. *Correspondence e-mail: chris.ling@sydney.edu.au

The Type II phase in the Bi$_{1-x}$W$_x$O$_{1.5+1.5x}$ system is shown to have a (3 + 3)-dimensional modulated δ-Bi$_2$O$_3$-related structure, in which the modulation vector ε 'locks in' to a commensurate value of 1/3. The structure was refined in a $3 \times 3 \times 3$ supercell against single-crystal Laue neutron diffraction data. *Ab initio* calculations were used to test and optimize the local structure of the oxygen sublattice around a single mixed Bi/W site. The underlying crystal chemistry was shown to be essentially the same as for the recently refined (3 + 3)-dimensional modulated structure of Type II Bi$_{1-x}$Nb$_x$O$_{1.5+x}$ (Ling *et al.*, 2013), based on a transition from fluorite-type to pyrochlore-type *via* the appearance of W$_4$O$_{18}$ 'tetrahedra of octahedra' and chains of corner-sharing WO$_6$ octahedra along $\langle 110 \rangle_F$ directions. The full range of occupancies on this mixed Bi/W site give a hypothetical solid-solution range bounded by Bi$_{23}$W$_4$O$_{46.5}$ ($x = 0.148$) and Bi$_{22}$W$_5$O$_{48}$ ($x = 0.185$), consistent with previous reports and with our own synthetic and analytical results.

1. Introduction

The search for new and improved solid-state oxide ionic conductors that show appreciable conductivity at moderate temperatures (773–973 K), for applications such as fuel-cell membranes, is one of the most important drivers of research in materials chemistry. The cubic phase of bismuth oxide, δ-Bi$_2$O$_3$, is the best-performing material at high temperatures, with oxide ionic conductivity of 1–1.5 S cm^{-1} at 1003–1103 K (Takahashi & Iwahara, 1978; Harwig & Gerards, 1978) owing to its disordered fluorite type (CaF$_2$) structure with 25% oxygen vacancies (Gattow & Schröder, 1962). However, δ-Bi$_2$O$_3$ is only stable above 1003 K, making it largely impractical as an ionic conductor. In order to stabilize δ-Bi$_2$O$_3$ to room temperature while preserving large parts of its conductivity, smaller rare earth or higher-valent transition metal cations such as Nb^{5+}, Ta^{5+}, Cr^{6+}, Mo^{6+}, W^{6+} and Re^{7+} can be introduced as dopants for Bi^{3+}. Ionic conductivity research has focused on the rare earth stabilized phases, which have disordered structures and are better conductors, but which also tend to undergo structural phase transitions to lower symmetry forms on repeated heating cycles (Watanabe, 1990).

Work on the transition metal-stabilized phases has concentrated on their crystallography, where they are a rich source of novel modulated structures; most famously, the 'Type II' (3 + 3)-dimensional incommensurately modulated
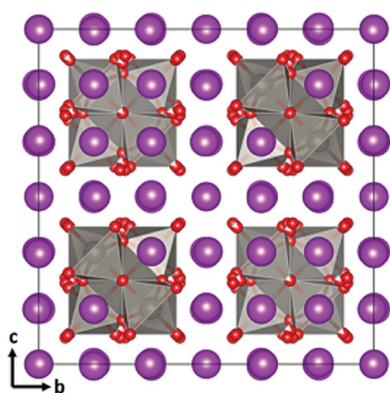
solid-solution phases. Examples include $Bi_{1-x}Nb_x^{5+}O_{1.5+x}$ (0.06 < x < 0.23; Ling *et al.*, 1998; Withers *et al.*, 1999; Ling *et al.*, 2013), $Bi_{1-x}Ta_x^{5+}O_{1.5+x}$ (0.1 < x < 0.25; Ling *et al.*, 1998; Struzik *et al.*, 2011), $Bi_{1-x}Cr_x^{6+}O_{1.5+1.5x}$ (0.05 < x < 0.15; Esmaeilzadeh *et al.*, 2001) and $Bi_{1-x}Mo_x^{6+}O_{1.5+1.5x}$ (0.05 < x < 0.15; Valldor *et al.*, 2000), which collectively represent the majority of known (3 + 3)-dimensional modulations. They have mainly been characterized by high-resolution transmission electron microscopy (HRTEM) and electron diffraction (ED), in trying to identify modulations by which the average fluorite substructure is distorted. The only full crystallographic refinement of a Type II phase was recently carried out by Ling *et al.* (2013) using single-crystal X-ray and neutron diffraction data.

Based on these studies, the crystal-chemistry of the Type II phases are thought to feature octahedral coordination environments of O atoms around the substituting metal atoms (M). These MO_6 octahedra are organized into chains along $\langle 110 \rangle_F$ directions (where the subscript F refers to the fluorite-type parent structure), which in turn intersect to form tetrahedral clusters of octahedra (Nb_4O_{18}), reminiscent of the pyrochlore structure type. The incommensurability reflects variability in the distance between MO_6 octahedral chains, which move apart in all four $\langle 110 \rangle_f$ directions as the M content decreases, maintaining cubic symmetry. The refined structure of Type II $Bi_{1-x}Nb_x^{5+}O_{1.5+x}$ (Ling *et al.* (2013) revealed these chains and clusters of NbO_6 octahedra, as well as isolated Nb sites with lower coordination numbers (NbO_5 and NbO_4) in the regions between the chains. However, the real-space resolution of the structure was limited by the number of modulation waves that could be refined, resulting in poorly defined coordination environments for Nb. In order to obtain a clearer picture of the local structure of the Type II phases, it would actually be preferable to find a commensurate version that could be solved and refined as a superstructure.

The search for a commensurate Type II phase led us to the $Bi_{1-x}W_x^{6+}O_{1.5+1.5x}$ system. Zhou (1994) investigated the Bi-rich end of this system using ED, HRTEM and X-ray powder diffraction (XRPD). This appears to be a high-temperature polymorph whose compositional range overlaps with that of the low-temperature Type Ib phase ($Bi_{1-x}W_x^{6+}O_{1.5+1.5x}$, $0.07 \le x \le 0.16$; Zhou, 1994; Watanabe *et al.*, 1985; Nespolo *et al.*, 2002; Sharma *et al.*, 2010), which has a tetragonal commensurate superstructure related to the fluorite-type parent structure by $\mathbf{a} = 2\mathbf{a}_F + \mathbf{b}_F$, $\mathbf{b} = -\mathbf{a}_F + 2\mathbf{b}_F$ and $\mathbf{c} = 2\mathbf{c}_F$. They reported that ED patterns for Type II samples in the compositional range from Bi_6WO_{12} (x = 0.143) to $Bi_{4.5}WO_{9.75}$ (x = 0.182) could be indexed to a $3 \times 3 \times 3$ commensurate face-centred cubic supercell of the δ-Bi_2O_3 structure. They proposed a preliminary structural model based on pyrochlore-like W_4O_{18} tetrahedral clusters, from which they simulated ED and HRTEM data that agreed reasonably well with experimental data. However, they also observed additional weak spots in the ED patterns, departing from face-centred symmetry, which could not be accounted for by the model. Due to the unavailability of single crystals, no further conclusions could be drawn.

Based on our recent success using the floating-zone method to grow large single crystals of Type II $Bi_{1-x}Nb_x^{5+}O_{1.5+x}$ (Ling *et al.*, 2013), we resolved to apply the method to samples in the compositional range of Type II $Bi_{1-x}W_x^{6+}O_{1.5+1.5x}$. The floating-zone method rapidly quenches the molten boule, which often leads to the growth of crystals of metastable high-temperature phases, as was the case for Type II $Bi_{1-x}Nb_x^{5+}O_{1.5+x}$. This suggested the possibility of obtaining a single-crystal sample of a Type-II phase with a commensurate $3 \times 3 \times 3$ superstructure, of sufficient size for an X-ray and/or neutron diffraction experiment.

2. Experimental

2.1. Synthesis

A single-phase polycrystalline sample of nominal composition of Bi_6WO_{12} was prepared by conventional solid-state synthesis in air. Stoichiometric amounts of WO_3 and Bi_2O_3 (Sigma Aldrich, > 99.999% purity) were ground in an agate mortar and pestle, pre-sintered at 1103 K for 1 h, reground and then sintered at 1123 K for 6 h. Samples were confirmed to be phase-pure tetragonal Type Ib (Zhou, 1994; Sharma *et al.*, 2010) by XRPD. Polycrystalline rods were pressed at 250 MPa in a hydrostatic press and sintered at 1173 K for 12 h. A crystal boule was grown by the optical floating-zone method using a Crystal Systems Corporation furnace (FZ-T-10000-H-VI-VP) equipped with 4×150 W halogen lamps. The boule was grown under a constant gas flow (20% O_2 in Ar) of 0.5 L min^{-1} at a rate of 2.5 mm h^{-1}, with constant counter-rotation of the feed and seed rod at 15 r.p.m. The resulting cylindrical boule had an average diameter of 6 mm and was bright yellow in colour, the upper half being transparent (Fig. 1).

Scanning electron microscopy (SEM) and energy dispersive X-ray (EDX) analysis were conducted at the Australian Microscopy and Microanalysis Facility (AMMRF) at the University of Sydney using a Zeiss EVO-50 Quenscan instrument with LaB_6 source. Results indicated that the composition of the grown boule in the region from which the crystal was taken was $Bi_{1-x}W_xO_{1.5+1.5x}$, x = 0.188, which is W-rich compared with the feed material Bi_6WO_{12} (x = 0.142). This deviation can be explained by the volatility of bismuth
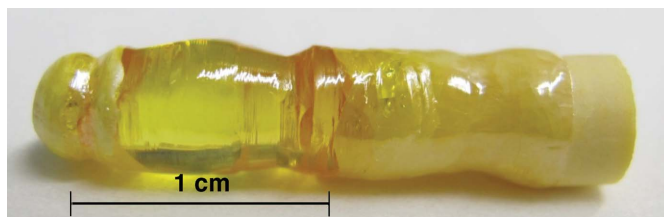
Figure 1
Floating-zone grown boule of nominal composition Bi_6WO_{12}. The polycrystalline seed rod can be seen at the right-hand end, followed by a multi-crystalline domain, a transparent single-crystal domain, and finally the frozen melt at the left-hand end. The average boule diameter is 6 mm.

Table 1
Crystal and refinement details.

Crystal data	
Chemical formula	$Bi_{23}W_4O_{46.5}$
Crystal system, space group	Cubic, $F\bar{4}3m$
Temperature (K)	298
a (Å)	16.6330 (15)
V (Å³)	4601.6 (7)
Z	4
Radiation type	Neutron, polychromatic
Crystal size (mm)	1.0
Crystal colour	Transparent yellow
μ (mm^{-1})	0.004
Data collection	
Diffractometer	Koala (ANSTO, Australia)
No. of measured, independent and observed [$I > 3\sigma(I)$] reflections	299, 187, 162
R_{int}	2.99
Refinement	
$R[F^2 > 3\sigma(F^2)]$, $wR(F^2)$, GOF	0.2490, 0.2732, 11.69
No. of reflections [$I > 3\sigma(I)$]	162
No. of parameters	21
No. of restraints	8

oxide, which was also noted in the synthesis of Type II $Bi_{1-x}Nb_x^{5+}O_{1.5+x}$ (Ling *et al.*, 2013).

2.2. Data collection and analysis

XRPD data were collected on a Panalytical X'Pert Pro diffractometer using Cu $K\alpha$ radiation.

HRTEM and ED data were collected using a Jeol 2100F transmission electron microscope on crushed grains of the powder sample dispersed onto holey carbon-coated copper grids.

Single-crystal X-ray diffraction data were collected at 150 K on a Bruker–Nonius APEX-II X-ray diffractometer with Mo $K\alpha$ radiation ($\lambda = 0.71073$ Å). 65 701 reflections could be indexed to a cubic unit cell with lattice parameter $a = 16.6330$ (15) Å (suggesting a $3 \times 3 \times 3$ superstructure of fluorite-type δ-Bi_2O_3) with the most probable space group $F\bar{4}3m$ (#216).

Single-crystal neutron Laue diffraction data at room temperature were collected using the instrument Koala at the OPAL research reactor, Lucas Heights, Australia. Koala uses a polychromatic neutron beam from the thermal neutron guide and is equipped with an image plate detector. An approximately spherical crystal fragment ~ 1 mm³ in volume was broken from the main crystal rod and mounted on an aluminium pin using fluorinated grease. The data collection consisted of 7 Laue images taken with a 3 mm diameter beam, 2 h exposures, and rotation steps of $40°$ perpendicular to the incident beam. Further experimental details are presented in Table 1.

The Koala detector covers $\sim 3\pi$ steradians in real space, but the coverage of reciprocal space is reduced as spots along the same direction in reciprocal space are overlapped for the Laue method. The software suite *LaueG* (R. Piltz, private comm.) was used to index, integrate (Wilkinson *et al.*, 1988) and apply wavelength normalization plus other intensity corrections

(Piltz, 2011) to obtain a list of integrated intensities. The satellite spots were indexed using the fractional Miller index $\varepsilon = 0.319$, with observed and calculated spot positions visually checked using the *LaueG* software. The main cell reflections (h,k,l) are surrounded by 8 first order satellites ($\pm\varepsilon,\pm\varepsilon,\pm\varepsilon$) and 18 second order satellites $\{(\pm2\varepsilon,\pm2\varepsilon,0), (\pm2\varepsilon,0,0),$ plus cyclic permutations$\}$. A total of 33 073 spots were integrated, of which 21 149 were accepted as being free from spot overlap and within the wavelength limits of 0.9–1.8 Å. After merging, 1157 unique reflections (including satellites) were obtained before space-group symmetry was considered.

Structure solution proceeded from the X-ray data using the charge flipping algorithm *SUPERFLIP* (Palatinus & Chapuis, 2007) with electron density extracted by the program *EDMA* (Palatinus *et al.*, 2012) as implemented in the *JANA*2006 software package (Petříček *et al.*, 2006), followed by difference Fourier maps using X-ray and neutron data in the commensurate approximation. All refinements were carried out using *JANA*2006.

2.3. *Ab initio* calculations

Ab initio density functional theory (DFT) calculations were performed using the Vienna *ab initio* simulation package (VASP; Kresse & Furthmüller, 1996; Kresse & Joubert, 1999). Calculations used the projector-augmented wave (PAW; Blöchl, 1994) method of Kohn-Sham DFT (Kohn & Sham, 1965) and the generalized gradient (GGA) approximation formulated by the Perdew–Burke–Ernzerhof (PBE) density functional (Perdew *et al.*, 1996, 1997). A cut-off energy of 400 eV (determined by oxygen) was chosen for the plane wave basis set. The Brillouin zone was sampled using a Monkhorst-Pack (111) k-point grid. Optimization of structural parameters was achieved using the conjugate gradient algorithm (Press *et al.*, 1986). All forces were relaxed below 0.01 eV Å^{-1}. Total energies were converged within 10^{-5} eV.

3. Results and discussion

3.1. Superspace symmetry considerations

Fig. 2 shows typical (*a*) $\langle 001 \rangle$ and (*b*) $\langle 110 \rangle$ zone-axis electron diffraction patterns (EDPs) of Type II $Bi_{1-x}W_xO_{1.5+1.5x}$, with selected reflections indexed in both $(3 + 3)$-dimensional modulated and $3 \times 3 \times 3$ superstructure notation. The average structure appears to be of oxygen-deficient fluorite type, space-group symmetry $Fm\bar{3}m$ ($\mathbf{a}_F$, $\mathbf{b}_F$, $\mathbf{c}_F$), where the subscript F refers to the average fluorite-related substructure. The satellite reflections can be indexed in $(3 + 3)$-dimensional notation by the basis vectors $\mathbf{a}_F^*$, $\mathbf{b}_F^*$, $\mathbf{c}_F^*$, $\mathbf{q}_1 = \varepsilon\mathbf{a}_F^*$, $\mathbf{q}_2 = \varepsilon\mathbf{b}_F^*$ and $\mathbf{q}_3 = \varepsilon\mathbf{c}_F^*$, where the parameter ε appears to be very close to $\frac{1}{3}$. Note the presence in Fig. 2 of very weak reflections that violate the F-centring extinction condition $F([hklmnp]^*) = 0$ unless $h + k$, $k + l$, $h + l$, $m + n$, $n + p$, $m + p$ are all even; and of weak structured diffuse scattering in the (001) plane. We will return to these observations in §3.2.

The fluorite-type parent structure contains three sites per primitive unit cell: a fully occupied metal ion M at 000

energy materials

[average atomic scattering factor $f_M^{av} = (1 - x)f_{Bi} + xf_W$]; and two partially occupied oxygen ions, O1 at $(\frac{1}{4}, \frac{1}{4}, \frac{1}{4})$ and the inversion symmetry related O2 at $(-\frac{1}{4}, -\frac{1}{4}, -\frac{1}{4})$ [average scattering factors $f_O^{av} = (1.5 + x)f_O$].

The three-dimensional compositional and displacive atomic modulation functions (AMFs) describing the perturbations away from the average occupancies and positions depend upon $(\mathbf{r}\mu + \mathbf{T})$. The position of the μth ion ($\mu = M$, O1 or O2) in the $\mathbf{T}$th unit cell [$\mathbf{T} = u \cdot \frac{1}{2}(\mathbf{a}_F + \mathbf{b}_F) + v \cdot \frac{1}{2}(\mathbf{b}_F + \mathbf{c}_F) + w \cdot \frac{1}{2}(\mathbf{c}_F + \mathbf{a}_F)$; u, v, w integers] of the average structure can be written as

$$\delta f_\mu(\mathbf{r}_\mu + \mathbf{T}) = f_\mu^{av} \Sigma_{mnp} a_\mu(mnp) \cos\{2\pi(m\varepsilon\mathbf{a}^* + n\varepsilon\mathbf{b}^* + p\varepsilon\mathbf{c}^*) \times (\mathbf{r}_\mu + \mathbf{T}) + \theta_\mu(mnp)\} \quad (1)$$

and

$$\mathbf{u}_\mu(\mathbf{r}_\mu + \mathbf{T}) = \Sigma_{\mathbf{\alpha}=\mathbf{a},\mathbf{b},\mathbf{c}}\Sigma_{mnp}\mathbf{\alpha}\varepsilon_{\mu\alpha}(mnp) \cos\{2\pi(m\varepsilon\mathbf{a}^* + n\varepsilon\mathbf{b}^* + p\varepsilon\mathbf{c}^*) \times (\mathbf{r}_\mu + \mathbf{T}) + \theta_{\mu\alpha}(mnp)\}, \quad (2)$$

respectively, where m, n and p are integers and label the particular modulation wave harmonic. Note that $a_\mu(-m, -n, -p) = a\mu(mnp)$, $\theta_\mu(-m, -n, -p) = -\theta_\mu(mnp)$, $\varepsilon_{\mu\alpha}(-m, -n, -p) = \varepsilon_{\mu\alpha}(mnp)$, $\theta_{\mu\alpha}(-m, -n, -p) = -\theta_{\mu\alpha}(mnp)$ *etc.* Determination of the above modulation wave amplitudes and phases essentially constitutes structure solution and refinement.

In the language of superspace, the desired resultant fractional coordinates in three-dimensional physical space, *i.e.* the *x*, *y*, *z* components of $(\mathbf{r}_\mu + \mathbf{T} + \mathbf{u}_\mu(\mathbf{r}_\mu + \mathbf{T}))$, are labelled x_1, x_2 and x_3, respectively. The corresponding perpendicular space fractional coordinates are given by $x_4 = \varepsilon\mathbf{a}^* \cdot (\mathbf{r}_\mu + \mathbf{T} + \mathbf{u}_\mu(\mathbf{r}_\mu + \mathbf{T}))$, $x_5 = \varepsilon\mathbf{b}^* \cdot (\mathbf{r}_\mu + \mathbf{T} + \mathbf{u}\mu(\mathbf{r}_\mu + \mathbf{T}))$ and $x_6 = \varepsilon\mathbf{c}^* \cdot (\mathbf{r}_\mu + \mathbf{T} + \mathbf{u}_\mu(\mathbf{r}_\mu + \mathbf{T}))$, respectively. [Note that the compositional and displacive AMFs of equations (1) and (2) are direct functions of $x_4^{av} = \mathbf{q}_1 \cdot (\mathbf{r}_\mu + \mathbf{T}) = \varepsilon\mathbf{a}^* \cdot (\mathbf{r}_\mu + \mathbf{T})$, $x_5^{av} = \mathbf{q}_2 \cdot (\mathbf{r}_\mu + \mathbf{T}) = \varepsilon\mathbf{b}^* \cdot \mathbf{r}_\mu + \mathbf{T})$ and $x_6^{av} = \mathbf{q}3 \cdot (\mathbf{r}_\mu + \mathbf{T}) = \varepsilon\mathbf{c}^* \cdot (\mathbf{r}_\mu + \mathbf{T})$,

respectively.] Superspace symmetry is expressed in terms of the effect of the particular symmetry operation upon fractional coordinates $\{x_1, \ldots, x_6\}$.

The ED data in Fig. 2 suggest that the appropriate (3 + 3)-dimensional superspace group is very close to $P:Fm\overline{3}m:Fm\overline{3}m$, implying $F([hklmnp]^*) = 0$ unless $h + k$, $k + l$, $h + l$, $m + n$, $n + p$, $m + p$ are all even. The generating elements of this superspace group ($P:Fm\overline{3}m:Fm\overline{3}m$) can be taken to be $\{x_1 + \frac{1}{2}, x_2 + \frac{1}{2}, x_3, x_4, x_5, x_6\}$, $\{x_1, x_2 + \frac{1}{2}, x_3 + \frac{1}{2}, x_4, x_5, x_6\}$, $\{x_1, x_2, x_3, x_4 + \frac{1}{2}, x_5 + \frac{1}{2}, x_6\}$ and $\{x_1, x_2, x_3, x_4, x_5 + \frac{1}{2}, x_6 + \frac{1}{2}\}$ for the lattice centring operations and $\{-x_1, x_2, x_3, -x_4 + 2\delta_1, x_5, x_6\}$, $\{x_1, x_2, -x_3, x_4, x_5, -x_6 + 2\delta_3\}$, $\{-x_1, -x_2, -x_3, -x_4 + 2\delta_1, -x_5 + 2\delta_2, -x_6 + 2\delta_3\}$, $\{x_2, x_1, x_3, x_5 + (\delta_1 - \delta_2), x_4 - (\delta_1 - \delta_2), x_6\}$ and $\{x_3, x_1, x_2, x_6 + (\delta_1 - \delta_3), x_4 + (\delta_2 - \delta_1), x_5 + (\delta_3 - \delta_2)\}$ for the rotational symmetry operations (Withers *et al.*, 1999).

For a truly irrational ε, the global phase parameters δ_1, δ_2 and δ_3 defining the initial phases of the AMFs can be freely chosen. However, if the parameter ε 'locks in' to a rational value, which it appears to do in the current case at $\frac{1}{3}$, the parameters δ_1, δ_2 and δ_3 become structurally significant in that they determine the conventional resultant three-dimensional space-group symmetry. For example, if $\delta_1 = \frac{1}{12}(u + w)$, $\delta_2 = \frac{1}{12}(u + v)$ and $\delta_3 = \frac{1}{12}(v + w)$, where u, v and w are integers, then the resultant superstructure will contain an inversion centre but not if otherwise. If u, v and w are all even, then the inversion centre is on a metal ion. If not, then the inversion centre is located midway between neighbouring metal ion sites but also midway between neighbouring oxygen ion sites, *e.g.* at $\frac{1}{4}(\mathbf{a}_F + \mathbf{b}_F)$. Likewise, if $\delta_1 = \delta_2 = \delta_3 = 0$, the resultant three-dimensional space group is $Fm\overline{3}m$. On the other hand, if $\delta_1 = \delta_2 = \delta_3 = \pm\frac{1}{12}$, then the resultant three-dimensional space group becomes $F\overline{4}3m$. Given the $m\overline{3}m$ symmetry of the experimental diffraction data, it is not possible to distinguish between these two possibilities. However, from the crystal chemical point of view, where W_4O_{18} tetrahedral clusters are the likely structural motif by analogy to Type II $Bi_{1-x}Nb_xO_{1.5+x}$ (Ling *et al.*, 2013), the latter $F\overline{4}3m$ three-dimensional space-group symmetry is the more likely.

3.2. Crystal chemistry, structural modelling and refinement

A question that must be considered before attempting to solve the structure is whether the modulation is commensurate or incommensurate. In our ED patterns (Fig. 2), the satellite reflections are asymmetric – the majority of the intensity appears to be centred on $\varepsilon = 1/3$, with a streaked 'tail' responsible for the shifted centre of mass. This suggests a slight incommensur-
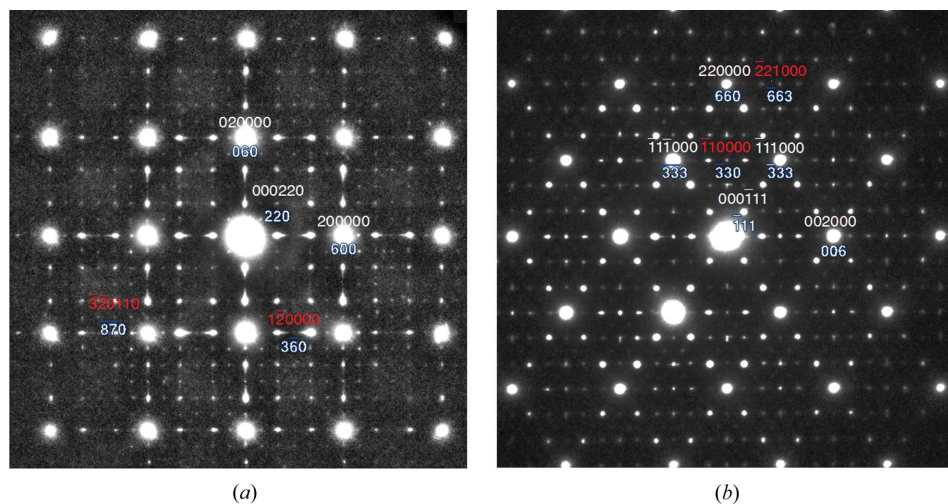
Figure 2
(*a*) $\langle 001 \rangle$ and (*b*) $\langle 110 \rangle$ zone axis EDPs of Type II $Bi_{1-x}W_xO_{1.5+1.5x}$. Selected reflections are indexed in (3 + 3)-dimensional notation (above the reflections) and $3 \times 3 \times 3$ supercell notation (below the reflections). The weak reflections labelled in red break the *F*-centring extinction condition. Note the presence of weak structured diffuse scattering in (*a*).

Table 2
Final refined fractional atomic coordinates, atomic displacement parameters and bond-valence sums (experimental and computational) for the refined structure of $Bi_{23}W_4O_{46.5}$, as well as average BVS for the equivalent sites in computational models W4, W4.5 and W5.

Atom	x (a)	y (b)	z (c)	U_{iso} (Å^2)	Frac. occ.	BVS (exp)	BVS (calc) W4	BVS (calc) W4.5	BVS (calc) W5
W	0.669 (2)	0.831 (2)	0.831 (2)	0.020 (4)	1	3.71 (17)	5.77	5.75	5.73
Bi1	0.0015 (11)	0.8372 (5)	0.8372 (5)	0.020 (4)	1	2.38 (8)	2.88	2.91	2.97
Bi2	0.5	0	0.8356 (11)	0.020 (4)	1	3.09 (11)	2.81	2.83	2.89
Bi3	0.3320 (9)	0.8320 (9)	0.8320 (9)	0.020 (4)	1	4.28 (13)	2.60	2.54	2.57
Bi, W4	0.5	0.5	0	0.020 (4)	1,0	2.20 (5)	2.89	2.67, 5.65	5.63
O1	0.9113 (12)	0.9113 (12)	0.9113 (12)	0.006 (8)	1	2.01 (7)	1.76	1.77	1.81
O2	0.0861 (18)	0.9139 (18)	0.9139 (18)	0.010 (10)	0.75	2.13 (10)	2.23	2.15	2.23
O3	0.4166 (13)	0.9166 (13)	0.761 (2)	0.062 (10)	1	1.75 (7)	1.94	1.97	1.99
O4	0.25	0.75	0.75	0.062 (10)	1	1.93 (4)	2.16	2.00	1.90
O5	0.628 (3)	0.75	0.75	0.072 (10)	1	1.67 (11)	1.87	1.85	1.84
O6	0.726 (3)	0.9142 (16)	0.9142 (16)	0.072 (10)	1	1.54 (9)	1.90	1.87	1.84
O7	0.25	0.099 (4)	0.25	0.062 (10)	0.75	1.83 (10)	1.88	1.91	2.00
O8	0.410 (2)	0.910 (2)	0.910 (2)	0.062 (10)	1	1.80 (9)	1.62	1.67	1.74

ability ($\varepsilon = 0.32$ rather than 1/3). However, the 'tail' does not index well to a second-order satellite reflection as would be expected if the structure is truly incommensurate. The HRTEM image shown in Fig. 3(a) sheds light on this by revealing that the crystal consists of large commensurate ($3 \times 3 \times 3$ fluorite subcell) regions, with occasional (00l) defect planes. A fast Fourier transform of this region reproduces both the satellites at $\varepsilon = 1/3$ and the diffuse streaking along (00l)*, as observed in Fig. 2, which serve to shift their apparent position slightly away from $\varepsilon = 1/3$. Based on these data it was clear that the local structure of Type II $Bi_{1-x}W_xO_{1.5+1.5x}$ would be more accurately treated as a commensurate $3 \times 3 \times 3$ supercell than as an incommensurate modulated structure.

Visual inspection of our single-crystal X-ray diffraction data indicated that they were badly compromised at the integration step by the presence of these asymmetric tails. Furthermore, even in the case of high-quality data, X-ray diffraction offers poor contrast between Bi (atomic number 83) and W (atomic number 74), both of which dominate the contribution of O (atomic number 8). In view of this, structure solution and refinement were carried out exclusively against neutron diffraction data, where the integration problems were simplified by the lower resolution; the relative neutron scattering lengths (Bi = 8.532, W = 4.86, O = 5.803 fm) also offered both better contrast between Bi and W, and better sensitivity to O in the presence of the heavy metals.

The neutron Laue diffraction data were transformed from the incommensurate indices used for integration to a commensurate $3 \times 3 \times 3$ subcell. The unit cell determined by single-crystal X-ray diffraction was used, given that white-beam Laue data cannot be used to refine a unit cell. Extinction conditions in this transformed data set were consistent with the $F\bar{4}3m$ space group.

The charge-flipping method immediately yielded the expected $3 \times 3 \times 3$ fluorite-type metal-atom array. These sites were initially assigned to Bi, then their relative occupancies refined one by one. On the basis of this, a site forming a cluster about a -4 symmetry element was clearly identified as W. Fourier difference maps revealed clearly defined O sites (labelled O5 and O6) around the cluster of four W sites (all crystallographically equivalent), together forming a tetrahedron of WO_6 octahedra (W_4O_{18}) reminiscent of the main structural motif refined in Type II $Bi_{1-x}Nb_xO_{1.5+x}$ by Ling *et al.* (2013) and originally proposed for this phase by Zhou (1994). Other O sites emerging from the Fourier difference map filled the remaining fluorite-type positions until the stoichiometry reached $Bi_{23}W_4O_{49}$. This composition is slightly O-rich relative to the charges on the cations, indicating the presence of O vacancies in the Bi-rich regions of the structure. Allowing O fractional occupancies to refine led us to reduce the occupancies of O2 and O7 to 75%,
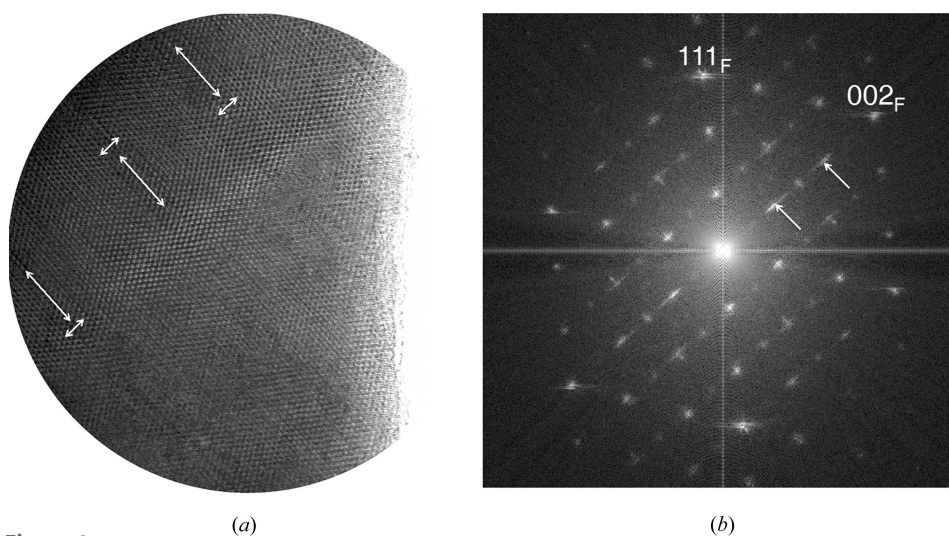

(a)
(b)

Figure 3
(a) High-resolution transmission electron micrograph perpendicular to $\langle 220 \rangle_F$, showing (00l) stacking faults indicated by arrows. (b) Fast Fourier transform of (a), showing diffuse streaking along (00l)* due to these faults (cf. Fig. 2a).

yielding a charge-balanced stoichiometry $Bi_{23}W_4O_{46.5}$. This structure refined stably, with atomic displacement parameters (ADPs) for the metal atoms, O5 and O6 (in the W_4O_{18} clusters), O1 and O2 (around the Bi4 site), and for the remaining fluorite-type O sites constrained together. The results are presented in Tables 1 and 2 and Fig. 4.

The relatively poor refinement statistics are partly a consequence of the neutron white-beam Laue method, in which the intensities of reflections must be normalized to the incident neutron spectrum. This means that some apparently very strong reflections have extremely high relative errors, which is generally not the case for monochromatic diffraction. In addition to biasing the refinement statistics, another consequence of this is that it is inappropriate to treat reflections as unobserved based on a criteria such as $I < 3\sigma(I)$; therefore, such reflections were excluded entirely from our refinement. It is nevertheless clear from the standard deviations on refined parameters in Table 2, and from calculated bond valence sums (BVS; Brown, 1996), that the structure is only as a first approximation. Some further symmetry lowering and/or disorder remains to be accounted for.

The composition at this stage ($Bi_{23}W_4O_{46.5}$, or $x = 0.148$ in $Bi_{1-x}W_xO_{1.5+1.5x}$) is close to the Bi-rich boundary of the Type II solid solution reported by Zhou (1994; Bi_6WO_{12} or $x = 0.142$). This was also the nominal composition of the feed rod from which this crystal was grown. However, it is significantly lower than the W content determined by SEM/EDX ($x = 0.188$). Indeed, further occupancy refinements pointed strongly to the presence of W on the Bi4 site, which is furthest from the W_4O_{18} clusters (note that similar isolated Nb sites were also found for Type II $Bi_{1-x}Nb_xO_{1.5+x}$). Assigning Bi4 entirely to W would give a stoichiometry $Bi_{22}W_5O_{48}$ ($x = 0.185$) after adjustment of O occupancies for charge balance. These experimental results are consistent with the W-rich boundary of the Type II solid solution region reported by Zhou (1994; $Bi_{4.5}WO_{9.75}$ or $x = 0.182$).

A model cannot be constructed in $F\bar{4}3m$ with octahedrally coordinated W on the Bi4 site unless those octahedra are highly disordered. The symmetry can be preserved if the W is tetrahedrally coordinated, which is plausible noting that the composition of this phase is intermediate between $Bi_{14}WO_{24}$ (Ling, 2006; Crumpton et al., 2003; Spinolo & Tomasi, 1997; Ling et al., 1999), which has tetrahedrally coordinated W and Bi_2WO_6 (McDowell et al., 2006; Rae et al., 1991; Wolfe et al., 1969; Takahashi & Iwahara, 1973), which has octahedrally coordinated W. However, tetrahedral coordination requires that the O2 site be entirely vacant. This would yield an O-poor stoichiometry $Bi_{22}W_5O_{45}$ even if all other O sites were fully occupied. The charge-balanced composition $Bi_{22}W_5O_{48}$ would require O2 to be 75% occupied, raising the average coordination number of W on the Bi4 site to 7.

In view of these crystal-chemical considerations, it is clear the Bi4 site has mixed Bi/W occupancy, and consequently a disordered average O coordination environment. An observation in support of this is that if the W- and Bi-occupied instances of this single crystallographic site were located as far apart from one another as possible, as would be expected from charge considerations, then the F-centring of the unit cell would be weakly broken. This is consistent with the ED data shown in Fig. 2.

Unsurprisingly, attempts to resolve the O disorder around the Bi4 site by refinement against neutron diffraction data were unsuccessful. Further structural analysis therefore made use of ab initio calculations to gain insight into the local structure about the Bi4 site, as described in the next section.

3.3. Computational modelling

All calculations used a commensurate $3 \times 3 \times 3$ fluorite-type supercell with the experimental cubic lattice parameter $a = 16.633$ Å. The number of oxygen vacancies within the cell was chosen to obtain a charge-balanced system resulting in supercells containing a total number of between 294 and 300 atoms for $Bi_{23}W_4O_{46.5}$ and $Bi_{22}W_5O_{48}$ ($Z = 4$) respectively. Calculations were carried out in $P1$ space symmetry, but the unit-cell parameters were fixed at their cubic values.

Calculations at the Bi-rich end of this composition range were performed using the first approximate model obtained via superflip followed by difference Fourier map in the $F\bar{4}3m$ space group and a composition of $Bi_{23}W_4O_{46.5}$ (mixed O2 and O7 vacancies). Starting from a fully occupied model ($Bi_{92}W_{16}O_{196}$), several possible arrangements for the 10 required oxygen vacancies within the $3 \times 3 \times 3$ supercell were tested, distributing them on O2, O7 and mixed O2 and O7 positions in accordance with experimental results. After structural relaxation (convergence was typically achieved after about 200 ionic
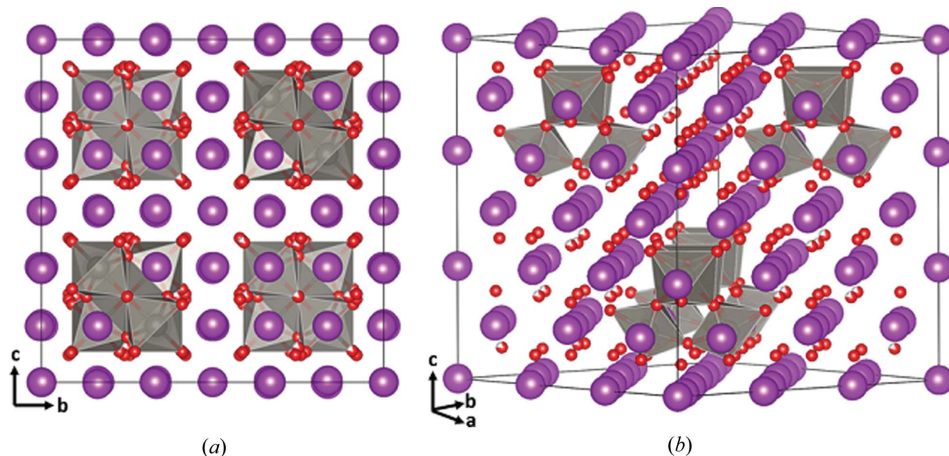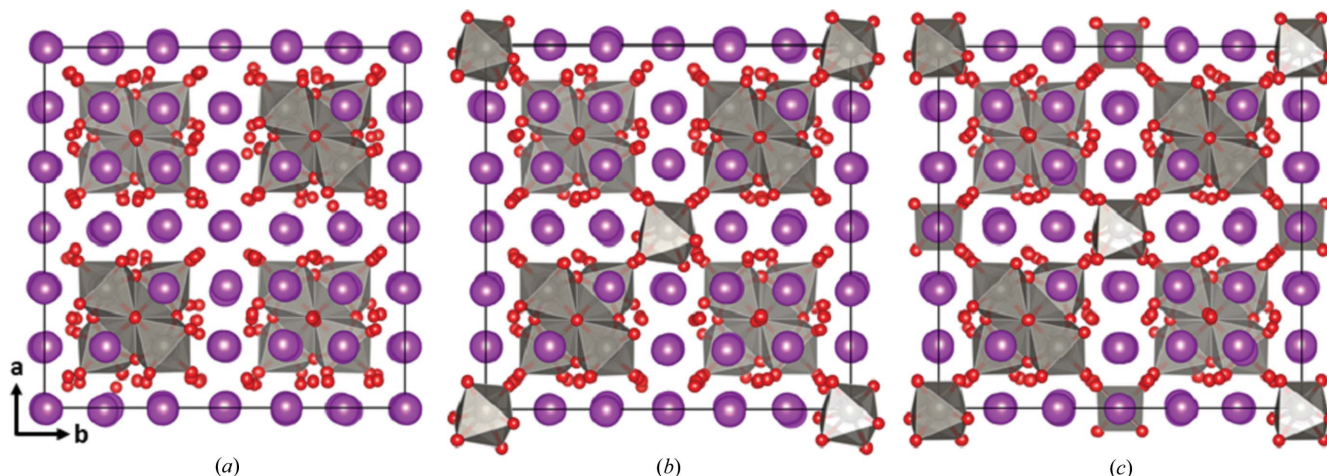

Figure 4
Final refined structure of Type II $Bi_{23}W_4O_{46.5}$ viewed (a) along [100] and (b) close to [$\bar{1}$10]. Bi atoms are purple, W atoms and polyhedra are grey, O atoms are red. Partial occupancies on O sites are indicated by coloured wedges.

Figure 5
Geometry optimized local structures of the three models for Type II obtained from *ab initio* calculations using a $3 \times 3 \times 3$ supercell of fluorite-type with symmetry removed: $Bi_{23}W_4O_{46.5}$ (*a*); $Bi_{22.5}W_{4.5}O_{47.25}$ (*b*) and $Bi_{22}W_5O_{48}$ (*c*). Bi atoms are purple, WO_6 polyhedra are grey, O atoms are red.

shifts), vacancies on the O2 position seem to be energetically favoured (-0.7 eV f.u.$^{-1}$ compared with mixed O2 and O7, -1.7 eV f.u.$^{-1}$ compared to O7 vacancies only). The best model obtained for this composition will hereafter be referred to as model W4 (Fig. 5*a*).

For higher W contents, as suggested by refinement against neutron data, the Bi4 site was occupied with 100% W atoms. For a charge-balanced stoichiometry, 4 vacancies had to be distributed amongst the O sublattice of the $3 \times 3 \times 3$ supercell. Several possible O distributions amongst all crystallographic oxygen positions were tested. As for $Bi_{23}W_4O_{46.5}$, the lowest energy was obtained with configurations containing O2 vacancies only (-1.6 eV f.u.$^{-1}$ compared with O7, -0.4 eV f.u.$^{-1}$ compared with O8 vacancies being the second best configuration after geometry optimization), in agreement with experimental results.

To obtain a better understanding of the local structure, further investigations then focused on different distributions of those vacancies amongst the O2 sublattice. Vacancy arrangements were classified by their grade of distribution (*i.e.* sum of distances between individual vacancies), with the general trend of higher distance sums resulting in lower energies. The best models all contained two vacancies each around two out of the four W atoms, leaving W in eight- and sixfold coordination environments, respectively. As the starting models all contained W on the Bi4 site, in eightfold cubic coordination, the main changes during structural relaxation occurred within these coordination environments. At positions without vacancies, structural relaxation results in WO_4 tetrahedra (4 O at a distance of 1.8 Å, 4 O > 2.6 Å), while starting in a sixfold coordination environment results in distorted WO_6 octahedra, hereafter referred to as model W5 (Fig. 5*c*).

In order to test the stability of model W5, the distorted WO_6 octahedra were manually transformed into regular octahedra and twisted randomly (check for false minima during geometry optimization). Structural relaxation rapidly returned the structure to the original model W5.

We then investigated the structure's ability to accommodate different W content, starting from $Bi_{23}W_4O_{46.5}$ and $Bi_{22}W_5O_{48}$ as hypothetical end-members of a solid solution range. In the $3 \times 3 \times 3$ supercell, only one intermediate charge balanced composition was possible, $Bi_{22.5}W_{4.5}O_{47.25}$, with mixed occupancy of 50% on the Bi4 site (Fig. 5*b*). Various models included different coordination environments for Bi and W according to model W4 and W5 for the end members as well as different possibilities of arranging additional oxygen atoms/vacancies.

Fig. 6 shows details of the different types of local O coordination around the crystallographically unique Bi4 site obtained in different parts of the computationally optimized cell, after symmetry has been removed to allow mixed Bi/W and partial O occupancy. It shows a variety of low-symmetry high-coordination number configurations around Bi4 sites (*a*, *b*), and regular octahedral (*c*) and tetrahedral (*d*) coordination around W4 sites. Fig. 6(*e*) shows an eightfold coordination of W in Model W5, where the cubic fluorite-type O sublattice has been strongly distorted to make four bonds much longer than
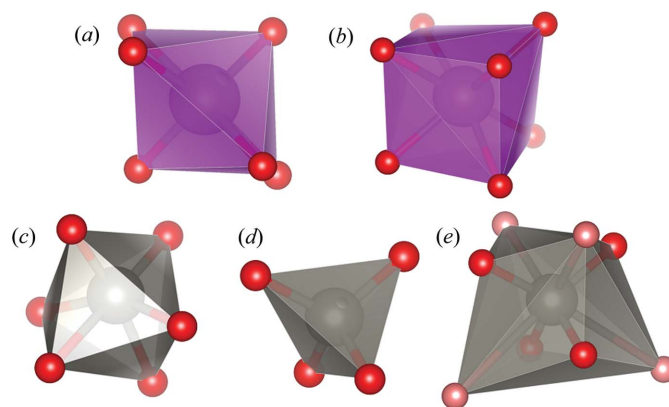
Figure 6
(*a*) Sixfold and (*b*) sevenfold coordination of Bi in Model W4.5. (*c*) Octahedral and (*d*) tetrahedral coordination of W in Model W4.5. (*e*) Eightfold coordination of W in Model W5.

the other four, so that the effective coordination environment is tetrahedral.

These results show that the structure can adapt very well to W^{6+}/Bi^{3+} substitution on the Bi4 site, whilst the W_4O_{18} 'tetrahedron of octahedra' on the W site are well defined (no significant changes during structural relaxations). All of our three computational models also show reasonable BVS for all crystallographic positions (Table 2), demonstrating that our models are all plausible representations of the local structure.

Finally, note in Fig. 5(c) ($Bi_{22}W_5O_{48}$, which corresponds most closely to the composition of our grown crystal as determined by SEM/EDX) that the W4 sites with tetrahedral and octahedral coordination are located as far apart from one another as possible, with the consequence that the F-centring of the unit cell is broken. This is consistent with the weak reflections observed in ED patterns, which were not included in the crystallographic average model.

4. Conclusions

Type II $Bi_{1-x}W_xO_{1.5+1.5x}$ is the first member of the family of $(3 + 3)$-dimensional modulated δ-Bi_2O_3-related phases where the modulation vector ε 'locks in' to a commensurate value, in this case, $\varepsilon = 1/3$. This permits a structure refinement in a $3 \times 3 \times 3$ supercell rather than as a modulated structure, which is an opportunity to test the validity of the recently refined modulated structure of Type II $Bi_{1-x}Nb_x^{5+}O_{1.5+x}$ (Ling *et al.*, 2013). The local crystal-chemistry of the two phases does indeed appear to be the same, dominated by the transition from fluorite-type to pyrochlore-type *via* the appearance of W_4O_{18} 'tetrahedra of octahedra' driven by the strong preference of W^{6+} for regular sixfold octahedral (or fourfold tetrahedral) coordination environments. Bi^{3+} supports much more irregular coordination environments due to spatial localization of the stereochemically active $6s^2$ electron lone pair. These W_4O_{18} clusters in turn form partial chains of corner-sharing WO_6 octahedra along $\langle 110 \rangle_F$ directions. Our model suggests the presence of additional W on the Bi4 site, resulting in a hypothetical solid-solution range bounded by $Bi_{23}W_4O_{46.5}$ ($x = 0.148$) and $Bi_{22}W_5O_{48}$ ($x = 0.185$). This range is consistent with previous reports and with our own synthetic and analytical results, and the presence of these additional sites is also consistent with our modulated structure model for Type II $Bi_{1-x}Nb_x^{5+}O_{1.5+x}$.

The long-range disordered nature of the Bi4 site limited our ability to resolve the local structure through refinement. We therefore used *ab initio* computational methods to test and optimize different possible models with symmetry removed. The results show that the structure adapts readily to W^{6+}/Bi^{3+} substitution on the Bi4 site, and that the W_4O_{18} 'tetrahedron of octahedra' is a very stable configuration. W on the Bi4 site was found to adopt both octahedral and tetrahedral coordination, with crystal-chemical arguments pointing to a 1:1 ratio at the W-rich end of the solid solution, $Bi_{22}W_5O_{48}$. Regular distribution of these two coordination environments would break the F-centring of the unit cell, something we observe experimentally in electron diffraction data.

These results present a clearer picture than ever before of the local structural environment of the modulated cubic δ-Bi_2O_3-related phases. One remaining issue is the presence of a relatively high concentration of (001) plane stacking faults, observed in high-resolution transmission electron microscopy and also manifest in a slight apparent incommensurability in diffraction data. It is not clear whether these are necessary to achieve the required oxygen stoichiometry across the solid solution range, or are simply a consequence of rapid quenching of the boule in the floating-zone furnace used to grow the crystals of this metastable phase. Future work will include an *in situ* high-temperature diffraction study to see if these stacking faults can be annealed out, as well as to explore the relationship to the low-temperature Type Ib phase of $Bi_{1-x}W_xO_{1.5+1.5x}$, which is reported to exist across approximately the same compositional region.

References

Blöchl, P. E. (1994). *Phys. Rev. B*, **50**, 17953–17979.
Brown, I. D. (1996). *J. Appl. Cryst.* **29**, 479–480.
Crumpton, T. E., Francesconi, M. G. & Greaves, C. (2003). *J. Solid State Chem.* **175**, 197–206.
Esmaeilzadeh, S., Lundgren, S., Hålenius, U. & Grins, J. (2001). *J. Solid State Chem.* **156**, 168–180.
Gattow, G. & Schröder, H. (1962). *Z. Anorg. Allg. Chem.* **318**, 176–189.
Harwig, H. A. & Gerards, A. G. (1978). *J. Solid State Chem.* **26**, 265–274.
Kohn, W. & Sham, L. J. (1965). *Phys. Rev.* **140**, A1133–A1138.
Kresse, G. & Furthmüller, J. (1996). *Phys. Rev. B*, **54**, 11169–11186.
Kresse, G. & Joubert, D. (1999). *Phys. Rev. B*, **59**, 1758–1775.
Ling, C. D. (2006). *Physica B*, **385–386**, 193–195.
Ling, C. D., Schmid, S., Blanchard, P. E. R., Petříček, V., McIntyre, G. J., Sharma, N., Maljuk, A., Yaremchenko, A. A., Kharton, V. V., Gutmann, M. & Withers, R. L. (2013). *J. Am. Chem. Soc.* **135**, 6477–6484.
Ling, C. D., Withers, R. L., Schmid, S. & Thompson, J. G. (1998). *J. Solid State Chem.* **137**, 42–61.
Ling, C. D., Withers, R. L., Thompson, J. G. & Schmid, S. (1999). *Acta Cryst.* B**55**, 306–312.
McDowell, N. A., Knight, K. S. & Lightfoot, P. (2006). *Chem. Eur. J.* **12**, 1493–1499.
Nespolo, M., Watanabe, A. & Suetsugu, Y. (2002). *Cryst. Res. Technol.* **37**, 414–422.
Palatinus, L. & Chapuis, G. (2007). *J. Appl. Cryst.* **40**, 786–790.
Palatinus, L., Prathapa, S. J. & van Smaalen, S. (2012). *J. Appl. Cryst.* **45**, 575–580.
Perdew, J. P., Burke, K. & Ernzerhof, M. (1996). *Phys. Rev. Lett.* **77**, 3865–3868.
Perdew, J. P., Burke, K. & Ernzerhof, M. (1997). *Phys. Rev. Lett.* **78**, 1396.

Petříček, V., Dušek, M. & Palatinus, L. (2006). *JANA*2006. Institute of Physics, Praha, Czech Republic.

Piltz, R. (2011). *Acta Cryst.* A**67**, C155.

Press, W. H., Flannery, B. P., Teukolsky, S. A. & Vetterling, W. T. (1986). *Numerical Recipes.* New York: Cambridge University Press.

Rae, A. D., Thompson, J. G. & Withers, R. L. (1991). *Acta Cryst.* B**47**, 870–881.

Sharma, N., Macquart, R. B., Avdeev, M., Christensen, M., McIntyre, G. J., Chen, Y.-S. & Ling, C. D. (2010). *Acta Cryst.* B**66**, 165–172.

Spinolo, G. & Tomasi, C. (1997). *Powder Diffr.* **12**, 16–19.

Struzik, M., Malys, M., Wrobel, W., Abrahams, I., Krok, F. & Dygas, J. R. (2011). *Solid State Ionics*, **202**, 22–29.

Takahashi, T. & Iwahara, H. (1973). *J. Appl. Electrochem.* **3**, 65–72.

Takahashi, T. & Iwahara, H. (1978). *Mater. Res. Bull.* **13**, 1447–1453.

Valldor, M., Esmaeilzadeh, S., Pay-Gomez, C. & Grins, J. (2000). *J. Solid State Chem.* **152**, 573–576.

Watanabe, A. (1990). *Solid State Ionics*, **40–41**, 889–892.

Watanabe, A., Ishizawa, N. & Kato, M. (1985). *J. Solid State Chem.* **60**, 252–257.

Wilkinson, C., Khamis, H. W., Stansfield, R. F. D. & McIntyre, G. J. (1988). *J. Appl. Cryst.* **21**, 471–478.

Withers, R. L., Ling, C. D. & Schmid, S. (1999). *Z. Kristallogr.* **214**, 296–304.

Wolfe, R. W., Newnahm, R. E. & Kay, M. I. (1969). *Solid State Commun.* **7**, 1797–1801.

Zhou, W. (1994). *J. Solid State Chem.* **108**, 381–394.